Geothermics 89 (2021) 101944

Contents lists available at ScienceDirect

Geothermics

journal homepage: www.elsevier.com/locate/geothermics

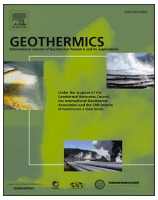

Thermo-mechanical tensile testing of geothermal casing materials

Gaute Gruben [a,*], Bert Dillingh [b], Gunnar Skúlason Kaldal [c], Nguyen- Hieu Hoang [a], Jens Wollenweber [b], Gisle Rørvik [d], Ingólfur Thorbjornsson [c], Bård Nyhus [a]

[a] *SINTEF Industry, Rich. Birkelands vei 2B, NO-7491 Trondheim, Norway*
[b] *TNO – Dutch Organization for Applied Research, the Netherlands*
[c] *ISOR – Iceland GeoSurvey, Grensásvegi 9, 108 Reykjavík, Iceland*
[d] *Equinor ASA, Arkitekt Ebbells veg 10, 7053 Ranheim, Norway*

ARTICLE INFO

Keywords:
Geothermal energy
casing materials
high-temperature engineering

ABSTRACT

Ultra-high temperature geothermal wells (>450 °C) have a large potential for increased energy yield as compared to conventional high-temperature geothermal wells (200-300 °C), but several research challenges must be resolved before robust operation in this temperature range can be achieved. In this study, yield- and tensile strength data for several relevant carbon steels and corrosion resistant alloys are generated as a step on the way to enable design of collapse- and tensile capacity for geothermal casings exposed to temperatures up to 500-550 °C. The experiments extend the data set listed in NZS 2403:2015 by providing data for higher temperatures and different material classes. It is found that the carbon steels follow the same near linear decay in strength as the NZS 2403:2015 curves up to 350 °C, and then display a significant drop in tensile strength at higher temperatures, particularly for the lower strength steels. The alloys with high nickel content work harden significantly more than the carbon steels at high temperatures and they tend to retain their strength at temperatures above 350 °C. The tested titanium alloy shows high yield strength and low work-hardening at 500 °C and in contrast to the tested nickel alloys, do not display dynamic strain ageing.

1. Introduction

Ultra-high-temperature geothermal wells (>450 °C) have a large potential for increased energy yield as compared to conventional high-temperature geothermal wells (200-300 °C) (Elders et al., 2014, Friðleifsson et al., 2014). Today's high-temperature geothermal wells with depths up to 3000 m are exposed to pressures and temperatures that are dominated by formation conditions and at highest follow the boiling point depth curve down to the critical point (374.15 °C and 221.2 bar for pure water) (Thórhallsson et al., 2014). Exceptions of the conditions exceeding the boiling depth curve have been seen in cases where the magma body is found at shallow depth and superheated conditions prevail. It follows that the main design code for geothermal wells, NZS 2403:2015 (New Zealand Standard, 2015), provides mechanical data for the relevant casing materials for temperatures up to 350 °C. For wells that can produce at supercritical conditions the temperatures and pressures are higher; for fresh water, the critical point is 374 °C and 221 bar, while for typical seawater the critical point is at 411 °C and 300 bar (Ingason et al., 2015, Knight and Bodnar, 1989). Since high-temperature geothermal wells still are under development, data on the mechanical properties of traditional casing materials and potential novel materials at elevated temperatures is not readily available.

Once wells heat up after they have been drilled, thermal expansion will lead to compressive stresses in the casings (Kaldal et al., 2015). In case some parts of the casing are not supported by cement, the compressive forces can result in elastic Euler buckling or local plastic buckling of the casing (Rechard and Schuler, 1983). In this respect, the temperature influence on the Young's modulus is of importance. Another concern during heating, is increased pressure on the outside of the casing due to heating of surrounding water if present. Downhole logging indicates that this can occur if the annular water is not vented sufficiently out to the rock formation, in particular between casings, or if the heating rate is too high (Kaldal et al., 2016, Kaldal, 2019). The pressure can be homogenous on the outside of the casing or it can occur locally due to a water pocket. In both cases, there is a risk of casing collapse. The casings collapse capacity is strongly linked to the yield strength of the material. Thus, it is critical to have good estimates of the casing materials yield strength at the design temperatures. If an

---

* Corresponding author.
E-mail address: gaute.gruben@sintef.no (G. Gruben).

https://doi.org/10.1016/j.geothermics.2020.101944
Received 1 May 2020; Received in revised form 28 July 2020; Accepted 22 August 2020

operating well must be shut down, the casing could be cooled over a short time period and as a result be exposed to large axial tensile stress. In a traditional geothermal well design, the casing segments are connected by threaded couplings, i.e. a rigid connection. It is of high importance that the designer knows the yield- and tensile strength of the materials for determining the elastic and the plastic design limit. It has been reported that novel design methods like the flexible coupling (Kaldal and Thorbjornsson, 2016, Thorbjornsson et al., 2017), can reduce axial compressive stresses during well warm-up and in turn reduce tension loads if wells get undesirable cool down, and keep the casing in the elastic domain. A different design strategy to mitigate high axial loads in such situations relies on the advance in material science technologies, e.g. development of corrosion resistant casing materials with low elastic Young's modulus and low thermal expansion. In this respect, titanium alloys, with about half Young's modulus and 67% thermal expansion in comparison with the carbon steels are promising. However, for any design in the ultra-high temperature range the designer is dependent on having access to relevant material data for such conditions.

For a specific geothermal well, the choice of casing material is strongly depending on the environmental loading the casing is exposed to. From the first well of the Icelandic Deep Drilling Project, IDDP-1, a microscopy study of carbon steel samples taken from the production casing near the well head showed cracks and fissuring (Thorbjornsson et al., 2020). These were likely to stem from high-temperature hydrogen attack and hydrogen embrittlement. Hydrogen assisted stress corrosion cracking was also observed in one of the samples taken from the outside of the casing near a leakage. Condensation from the steam was very acidic with pH around 3 due to generation of H + ions from HCl and HF (Ármannsson et al., 2014). In a different study from IDDP-1, Karlsdottir et al. (2015) investigated several alloys against corrosion in superheated geothermal steam at a temperature of 360 °C for 113 days. The study was conducted under conditions where no steam condensation was present, and they concluded that carbon steel could be used under these conditions. Based on the study by Thorbjornsson et al. (2020) and Karlsdottir et al. (2015) the application domain for carbon steel in superheated wells appears to be in areas where the material is not exposed to condensed steam. Carbon steels can potentially be used in casing for supercritical conditions, but only if a corrosion resistant clad material is applied to protect the carbon steel. Thus, mechanical data for Corrosion Resistant Alloys (CRA) that can withstand the environmental loading and can be applied as a casing or as cladding material is of high relevance in design of high-temperature geothermal wells.

In this study we provide yield- and tensile strength data for several relevant carbon steels and CRA materials. The data is provided as a step in enabling casing design, e.g. of casing collapse, burst and compressive/tensile capacity, for geothermal wells with temperatures between ambient and 500-550 °C, and so extend the basis given in NZS 2403:2015. The experimental data are obtained from cross-fertilization of two studies; one conducted at TNOs test laboratory in Eindhoven (NL) as part of the EU project GeoWell (2014-2018) and one from SINTEFs test laboratory in Trondheim (N) as part of the Norwegian innovation project HotCaSe (2017-2021). The experimental data from TNO was submitted as part of a publication for the WGT 2020 before the preparation of this manuscript, Dillingh et al. (2020). The WGC 2020 conference was postponed and related publications will become available in 2021.

2. Materials and test matrix

Table 1
Material test matrix. OD = outer diameter, WT = wall thickness. The T95 material tested in both laboratories is from the same casing.

Label	Material class	OD / WT	SINTEF	TNO	Geometry
K55A	Carbon steel	13-3/8″ / 12.2 mm	√		Ø8A
K55B	Carbon steel	13-3/8″ / 13.1 mm		√	Ø8C
L80	Carbon steel	9-5/8″ / 12.0 mm		√	Ø8C
T95	Carbon steel	9-7/8″ / 15.9 mm	√	√	Ø8A / Ø8C
P110	Carbon steel	9-7/8″ / 16.8 mm	√		Ø8A
600	Nickel based alloy	Plate / 12.4 mm	√		Ø6
625A	Nickel based alloy	Plate / 10.9 mm	√		Ø6
625B	Nickel based alloy	Plate / 13.8 mm		√	Ø8C
800	Nickel based alloy	Plate / 6.7 mm	√		Ø4
C276	Nickel based alloy	Plate / 10.0 mm	√		Ø6
6Mo	Austenitic stainless steel	6-5/8″ / 18.3 mm	√		Ø8A
Ti23	Titanium alloy	~30″ / 40 mm	√		Ø8B

The material test matrix can be divided into two main groups: carbon steel casing material and CRA casing materials. Table 1 gives an overview of the tested materials and the laboratory that performed tests on each specific material. The carbon steel group consist of four different casing material types: the low yield-tensile ratio steel K55, and the high yield-tensile ratio steels L80, T95 and P110. Testing on K55 was performed on materials from two different producers and these are labeled K55A and K55B in Table 1. Note that the T95 from the same casing segment was tested in both laboratories. The CRA casing materials consist of four types of nickel-based alloys, an austenitic stainless steel, and a titanium alloy as shown in Table 1. Note that testing on Inconel 625 have been performed with materials from two different producers and are labelled 625A and 625B in Table 1.

The tests conducted at SINTEF are performed at room temperature (RT), 350 °C and 500 °C, while the tests conducted at TNO are performed at RT, 250 °C, 450 °C and 550 °C. The chemical composition of each material is given in Table 2. Note that some of the compositions are based on ladle analysis, while other are from product analysis as marked in the table. The chemical composition of the carbon steels are within the specifications of API Spec 5CT (ISO 11960:2014(E)) (American Petroleum Institute, 2011), while the Nickel based alloys and the austenitic stainless steel have compositions within the Unified Numbering System (SAE and ASTM, 2017). The chemical composition of the titanium alloy was not provided and so a chemical analysis was conducted. The amount of the tested alloying elements are found to be within Grade 5 and Grade 23 as defined by ASTM B862 (ASTM International, 2019)[1] . Further, the strength properties were found to be within the specification of Grade 23 but did not meet the strength requirements for Grade 5. In the following we will refer to the titanium alloy as a Grade 23.

3. Experimental methods

3.1. Specimen geometry

Most of the tests are performed on specimens with an 8 mm nominal diameter. However, since the nickel-based alloys and the austenitic stainless steel tested in the SINTEF laboratory were delivered from plates with relatively small thickness, the specimen geometry on these tests are sub sized. In total four tensile test geometries denoted Ø8A, Ø8B, Ø6 and Ø4 from SINTEF applied in this study, while one tensile test geometry denoted Ø8C is applied in the tests from TNO. Fig. 1 shows the nominal specimen geometries of the tensile specimens. The relation between original gauge length and diameter is in accordance with ISO 6892 Part 1 and Part 2 (International Organization for Standardization, 2016, International Organization for Standardization, 2018) for all applied

---

[1] Note that the nitrogen content was not tested in the chemical analysis, and the content of oxygen is high but within the permissible variation in product analysis following ASTM B862 (+0.03%). The material was tested for ruthenium, but this element was not found and therefore this is not a Grade 29.

Table 2
Chemical components of the tested materials [in wt. %]. Superscript L indicate ladle analysis while P indicate product analysis.

	K55A^L	K55B^L	L80^P	T95^L	P110^L	600A^P	625A^P	625B^P	800^P	C276^P	6Mo^L	Ti23^P
C	0.32	0.34	0.33	0.27	0.26	0.05	0.06	0.05	0.70	0.003	0.014	0.01
Mn	1.20	1.38	1.42	0.63	0.83	0.28	0.33	0.08	0.60	0.50	0.72	
Si	0.24	0.27	0.31	0.19	0.27	0.26	0.16	0.07	0.30	0.02	0.29	
Cr	0.023	0.08		1.03	1.12	16.13	21.80	22.5	20.80	15.80	19.9	0.02
Mo	0.001	0.055		0.42	0.32		8.20	8.1		15.60	6.15	
S	0.009	0.0018	0.007	0.002	0.002	<0.001	<0.001	<0.001	<0.001	<0.001	0.0007	
P	0.014	0.012	0.018	0.010	0.014	0.009	0.01	0.005	0.17	0.01	0.024	
Ni	0.005	0.050	0.01	0.03		balance	balance	balance	balance	balance	17.8	0.01
Cu	0.043	0.115	0.01	0.05		0.01			0.08		0.66	
Al		0.015		0.023	0.036		0.30		0.30			5.7
Ti		0.011			0.006		0.19	0.3	0.30			balance
V		0		0.01						0.11		4.1
N		0.0059									0.1985	
As		0.004		0.0045								
Ca		0.0018										
Pb + Sn		0.007		0.0052								
Co							<0.1	0.1		0.20		
Nb							3.38	3.654				
Ta							0.010	0.004				
W										3.30		
O												0.16
H												0.01
Fe	balance	balance	balance	balance	balance	8.98	4.20	4.5	46.35	6.10	balance	0.14

specimens.

3.2. Test set-up and data processing

The tests conducted at the SINTEF laboratory are performed in an Instron 100 kN universal test machine, while heating of the specimens is facilitated by induction from a Hüttinger 40 kW generator and a Sigmatest/Eurotherm temperature controller. The test set-up is shown in Fig. 2. The tests are carried out under displacement control with a nominal strain-rate of $2.5 \cdot 10^{-4}$/s, which corresponds to range 2 following ISO 6892-1 (International Organization for Standardization, 2016). The test set-up is shown in Fig. 1. The inductive heating device is installed in the test machine and the copper coil is adjusted to the length of the test specimen. One thermocouple is spot welded to the specimen and connected to the temperature controller to adjust the heat input from the generator. An MTS extensometer, specifically made for induction heating with ceramic arms and heat shield, is used to measure the strain. The gauge length of the extensometer is 25 mm and the maximum travel is 2.5 mm.

Prior to testing, the diameter was measured at three locations along the gauge length at two angles, i.e. a total of 6 measurements were conducted on each specimen. The force, F, the extensometer displacement, u^{ext}, and the actuator displacement, u^{act} were logged at a frequency of 5 Hz. The average deviation from the nominal diameter, D_0, was less than 0.1% in all specimens and so the engineering stress, s, was calculated based on the nominal diameter for all tests as

$$s = F \big/ \left(\pi D_0^2 \big/ 4\right) \tag{1}$$

Since the extensometer reading was limited to a maximum value that in some cases occurred before onset of necking, A_{gt}, the engineering strains larger than 0.1 were calculated from the actuator displacement reading. To achieve good quality on the strains determined by the actuator displacement, a correction for the machine compliance was performed as (Albertini and Montagnani, 1977)

$$e^{corr} = e^{act} - s \cdot \frac{e_0^{act} - e_0^{ext}}{s_0} \tag{2}$$

Here, e^{act} is the engineering strain based on the actuator displacement and the specimen gauge length, while e^{corr} is the corrected strain. Further, e_0^{act} is the strain at initial yielding calculated from the actuator displacement, e_0^{ext} is the strain at initial yielding based on the extensometer reading, and s_0 is the engineering stress at initial yielding.

The tests conducted at the TNO laboratory are carried out in an MTS tensile rig with a capacity of 250 kN. To enable high temperature testing the rig is equipped with an oven capable of reaching temperatures of 1200 °C. Fig. 3(a) shows the tensile test rig and the oven. For measuring the strain at high temperatures, a special high-temperature Linear Variable Displacement Transducer (LVDT) is used, see Fig. 3(b). The LVDT is designed with the active measurement element outside the oven. The HT-LVDT design is such that the strain measurement is insensitive to temperature changes over a large temperature range. To be able to use these HT-LVDT's the tensile specimens require collars to fit the HT-LVDT's clamps. The temperature of the specimen is actively monitored using a type E thermocouple. Following ASTM E21 (ASTM International, 2017), the thermocouple's tip is shielded from direct radiation for accurate determination of the temperature, see Fig. 3(c).

The tests are carried out under displacement control with a nominal strain-rate of $2.0 \cdot 10^{-3}$/s, which corresponds to range 3 following ISO 6892-1 (International Organization for Standardization, 2016). The engineering stress are calculated from the force recordings and the nominal cross-section area following Equation (1) and the engineering strain are calculated from the LVDT displacement reading with a gauge length of 42 mm.

4. Results

The tests performed in this study are not designed for extracting high-quality measurements of the Young's modulus, and therefore this parameter will not be emphasized. However, to illustrate the range of the Young's modulus in the test matrix, the values from selected materials are presented in Fig. 4. The K55A material follows the trend of the carbon steels given in NZS 2403:2015 up to 350 °C, and then decrease with a higher rate up to 500 °C. The Young's modulus for the nickel based alloy 625A is ~35 GPa lower than for the K55A steel at room temperature and ~20 GPa higher than for K55A at 500 °C. The 6Mo stainless steel display a similar behavior as the nickel-based alloy but is more sensitive to increased temperature. The Ti23 alloy stand out, as it has a Young's modulus of 118 GPa at RT with a near linear decease to 95 GPa at 500 °C, and so display an elastic stiffness that is significantly lower than in the other materials.

In the case of investigation of the ductile fracture characteristics of the material, the post-necking response is of relevance. It was found that the neck developed differently with the induction heating and the

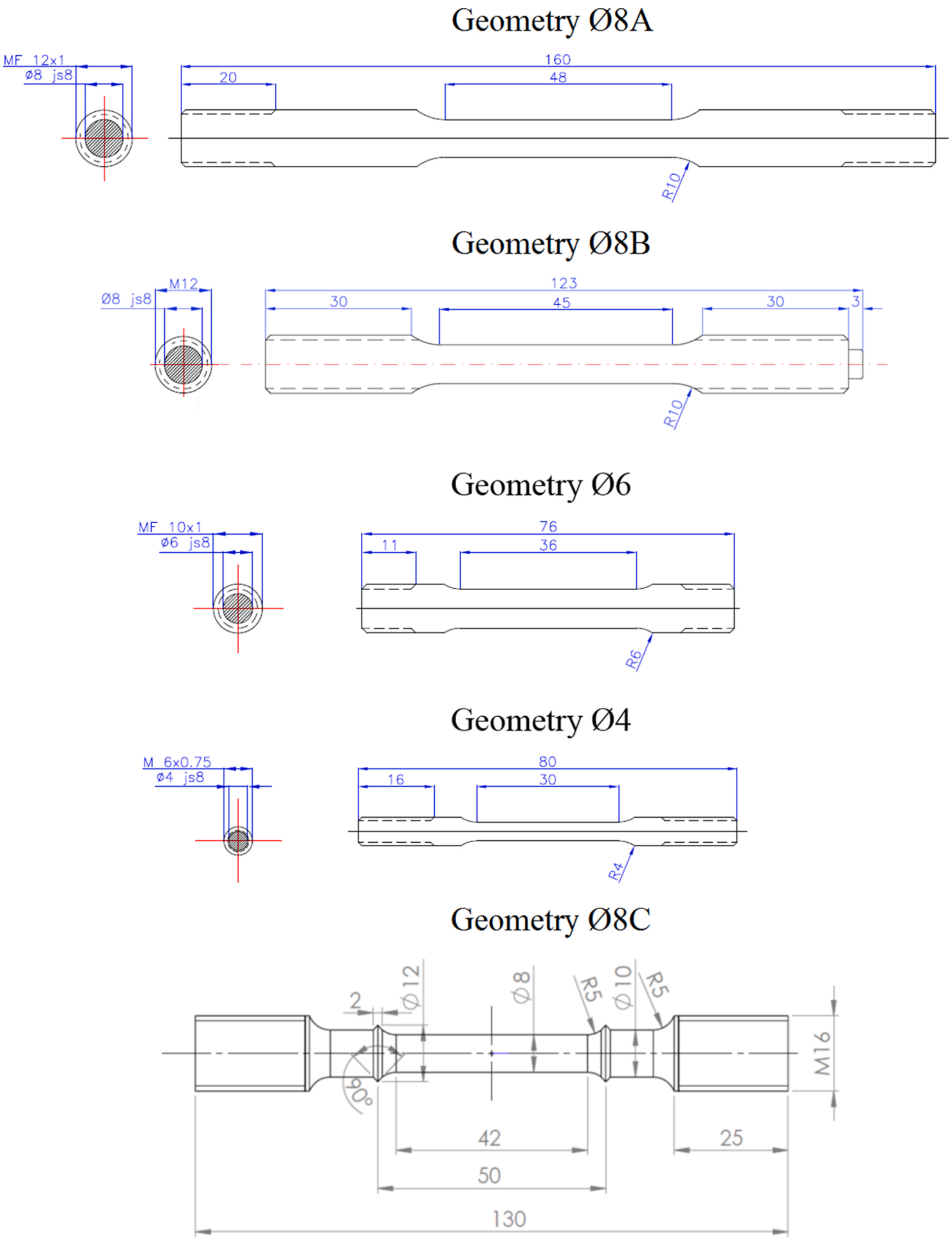

Fig. 1. Nominal tensile test geometries. The Ø8A, Ø8B, Ø6 and Ø4 geometries are applied at SINTEFs laboratory, while geometry Ø8C is applied at TNOs laboratory.

furnace heating procedure. Many influencing factors have been discussed and additional tests were run in an attempt to understand the differences. It was concluded that pursuing this would need a complete separate study. In the present study we aim to provide relevant data for design of collapse capacity during heating and tensile capacity during cooling of high-temperature geothermal wells. Thus, the focus will be on the material response from yielding to onset of necking. It is emphasised that the yield-strength in tension can be assumed to be similar to the yield strength in compression, see e.g. (Seely and Putnam, 1919). In the following sections, the engineering stress-strain curves until onset of necking (i.e. until the ultimate tensile strength) from the different materials are provided. From the engineering stress-strain curves the 0.2% non-proportional proof strength ($R_{p0.2}$), the tensile strength (R_m) and the engineering strain at necking (A_{gt}) are extracted. Based on the average values of $R_{p0.2}$, R_m and A_{gt}, the yield strength factor (YFS), the tensile strength factor (TSF) and the elongation factor (EF) are calculated. These factors are calculated by taking the ratio of a given parameter at a given temperature with the value of the same parameter at room temperature.

4.1. Carbon steels

All the tested carbon steels had yield- and tensile strength in accordance to API Spec 5CT (American Petroleum Institute, 2011), as pointed out in Section 2 the chemical composition also is within API Spec 5CT and follows that the tested carbon steels are representative of their respective class.

4.1.1. Carbon steel K55 (API Spec 5CT K55)

The K55A material tested in the SINTEF laboratory was provided by Shandong Molong Petroleum Machinery Co., Ltd. and came from a 13-3/8″ casing with a nominal wall thickness of 12.2 mm. The K55B material tested in the TNO laboratory were from a 13-3/8″ casing with a nominal wall thickness of 13.06 mm produced by Tenaris at Veracruz in Mexico. The casing tested at both labs were from hot-rolled pipe sections. The chemical composition of K55A and K55B is given in Table 2.

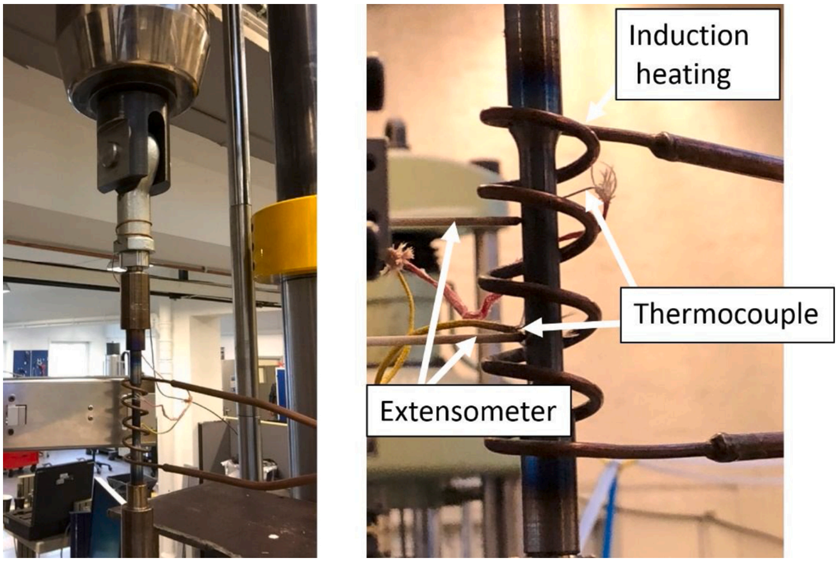

Fig. 2. Tensile test set-up at the SINTEF laboratory.

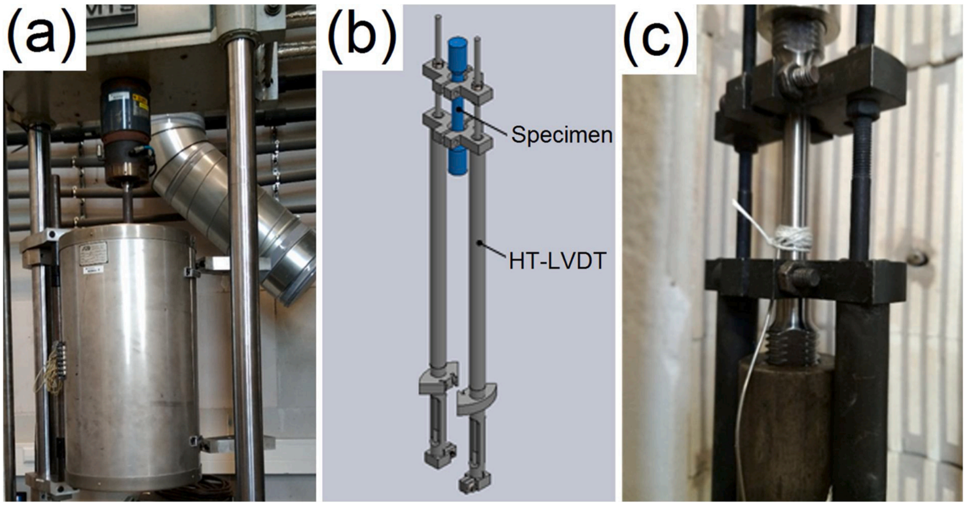

Fig. 3. Test set-up at the TNO laboratory. (a) MTS tensile rig with integrated oven. (b) Sketch of specimen and High-temperature Linear Variable Displacement Transducer. (c) Thermocouple fastened directly to the specimen.

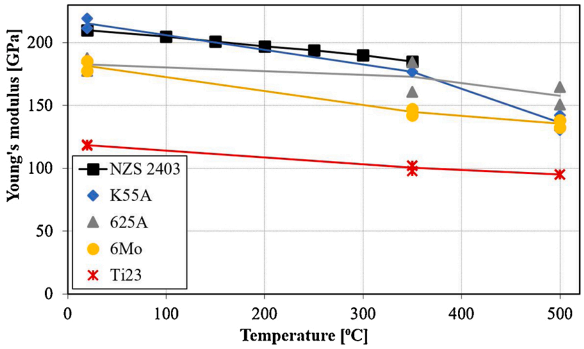

Fig. 4. Young's modulus from selected materials compared with data from NZS 2403:2015. Results from all parallels are shown together with trend lines for each material.

The engineering stress-strain curves until onset of necking for the K55A and K55B materials are shown in Fig. 5. At room temperature, the two materials have very similar strength, but the K55B material display a yield (Lüders) plateau. It follows that the resulting 0.2% proof strength is larger for K55B than K55A, but the stress level for strains above 0.01, including the tensile strength (R_m), is very similar for both materials. The presence of a Lüders plateau could stem from differences in chemical composition, microstructure or mechanical loading. The K55B steel contain nitrogen which can bind the dislocation movement. Further K55 is fully normalized, while the heat treatment of the K55A material is not specified in the material certificate. Finally, the strain-rate of the K55B tensile tests is 8 times higher than in the tensile tests of K55A. All these three factors can contribute to the presence of a Lüders plateau in K55B and not in K55A. According to the API 5CT (American Petroleum Institute, 2011) specifications, the K55 casing materials have a specified yield strength within the range 379-551 MPa, while the specified minimum tensile strength is 655 MPa. As can be seen from Table 3, both materials are within the API 5CT specifications. The total strain at necking (A_{gt}) is larger for the K55B material than for the K55A material within the tested temperature range. The yield plateau observed at room

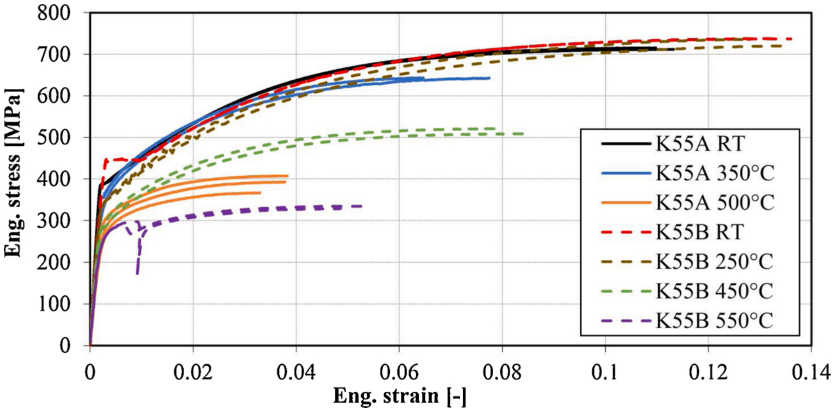

Fig. 5. Engineering stress-strain curves from all tensile tests on the K55A and K55B materials.

Table 3
Proof strength ($R_{p0.2}$), tensile strength (R_m), strain at onset of necking (A_{gt}) for the K55 materials. The yield strength factor (YSF), tensile strength factor (TSF) and elongation factor (EF) are given based on the average $R_{p0.2}$, R_m and A_{gt} values.

Material	Temp.	Parallel	$R_{p0.2}$	R_m	A_{gt}	YSF	TSF	EF
K55A	RT	1	397	716	0.110			
		2	398	712	0.113			
		Avg.	397	714	0.111	1.00	1.00	1.00
	350 °C	1	389	643	0.067			
		2	374	643	0.078			
		Avg.	381	643	0.072	0.96	0.90	0.65
	500 °C	1	288	367	0.033			
		2	305	393	0.038			
		3	314	407	0.038			
		Avg.	302	389	0.036	0.76	0.54	0.33
K55B	RT	1	443	738	0.134			
		2	444	737	0.136			
		Avg.	444	738	0.135	1.00	1.00	1.00
	250 °C	1	366	736	0.128			
		2	361	720	0.136			
		Avg.	364	728	0.132	0.82	0.99	0.98
	450 °C	1	319	509	0.085			
		2	320	521	0.081			
		Avg.	320	515	0.083	0.72	0.70	0.61
	550 °C	1	281	329	0.050			
		2	281	335	0.054			
		Avg.	281	332	0.052	0.63	0.45	0.38

temperature in the K55B material, disappear at higher temperatures as can been seen from the 250 °C and 450 °C tests. Though at 550 °C it re-appears once as a dip just beyond the yield point. In one of the parallels at 550 °C the dip is very deep. This is not believed to be the actual decrease but merely an artefact of the control system handling the quick changes in the specimen's response.

For increased temperature, the strength and the total elongation at necking is significantly reduced in the K55 tests, with an exception of the K55B material at 250 °C which have nearly the same A_{gt} and R_m as it has at room temperature, but a lower $R_{p0.2}$, mainly due to the lack of a yield plateau. The tests at 500 °C of the K55A material display a strength between the strength found at 450 °C and 550 °C of the K55B material, but again, the elongation at necking is smaller for the K55A material.

In conclusion both materials are within the API 5CT specifications

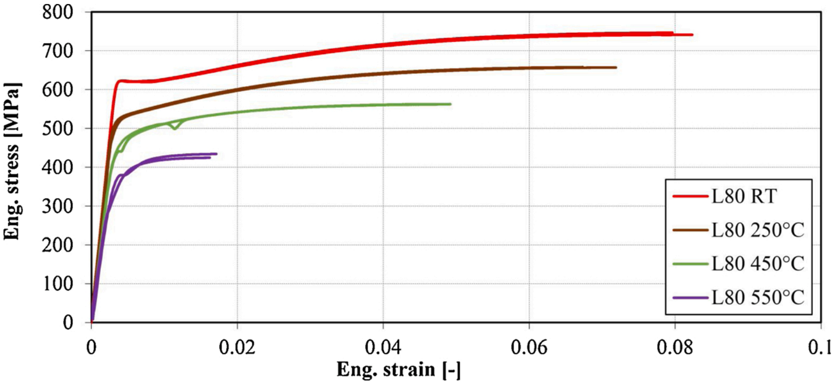

Fig. 6. Engineering stress-strain curves from all tensile tests on the L80 material.

and are thus considered representative K55 alloys. In contrast to the K55A material, the K55B material have a Lüders plateau, and the elongation at necking is larger in K55B. Both materials respond similarly to increased temperature.

4.1.2. Carbon steel L80 (API Spec 5CT L80)

The L80 material is produced by Jiangsu Changbao Steel Tube Ltd. Co. as a 9-5/8″ pipe with a nominal wall thickness of 11.99 mm. As can be seen from Fig. 6, a yield plateau is present in the room temperature parallels, but not in the tests at higher temperature. The proof- and tensile strength at room temperature given in Table 4 are within the API-5CT (American Petroleum Institute, 2011) standard for L80, i.e. 551 MPa $\leq R_{p0.2} \leq$ 655 MPa and $R_m >$ 655 MPa. The results between the parallels for each temperature are consistent, and a distinct reduction in both strength and elongation at necking is present for increased temperature. Especially the elongation at necking is reduced significantly when increasing the temperature from 450 °C to 550 °C. One of the parallels at 450 °C and 550 °C display kinks in the stress level. This is not believed to be the specimen's actual response, but rather an artefact of the control system.

4.1.3. Carbon steel T95 (API Spec 5CT T95)

Samples from the same section with T95 material was provided to the test laboratories at SINTEF and TNO. The seamless hot-rolled pipe section was produced in 2016 by Tianjin Pipe (Group) Corporation and had an outer diameter of 9-7/8" and a wall thickness of 15.8 mm. The chemical composition is given in Table 2. Following API-5CT (American Petroleum Institute, 2011), the T95 have a specified yield strength of 655-758 MPa and a minimum tensile strength of 724 MPa. As can be seen from Table 5 and indicated in Fig. 7, the room temperature tests at both test labs fulfil the strength requirement of the T95 in API-5CT, but the room temperature tests performed at SINTEF (T95A) have ~5 % lower strength than the tests performed at TNO (T95B). The difference in strength is likely due to the visco-plastic effect resulting from the difference in strain-rate. As pointed out in Section 3.2, the tests conducted at SINTEF had a strain rate at the lower bound of the ISO 6892-2 standard (International Organization for Standardization, 2018) ($2.5 \cdot 10^{-4}$/s), while the tests performed at TNO had strain rates in the upper bound ($2.0 \cdot 10^{-3}$/s). Both the T95A and the T95B tests display a distinct yield plateau up to a total strain of approximately 0.016. As with the K55B and L80 materials, the yield plateau is not present at higher temperatures. The total strain at necking (A_{gt}) is higher in the T95A tests (average $A_{gt} = 0.091$) than in the T95B tests (average $A_{gt} = 0.086$), and this is also assumed to stem from the difference in strain rate.

The T95 material displays a distinct reduction in strength and elongation at necking for increased temperature in both the T95A and T95B tests. The tendency of higher elongation in the T95A tests and higher strength in the T95B tests is also present at high temperatures as can be observed when comparing the T95A stress-strain curves at 500 °C with the T95B stress-strain curves at 550 °C. Here the T95B material have the same strength as the T95A material and both materials have the same elongation at necking even though the T95B material is tested at 50 °C higher temperature. The results from the T95A and T95B tests indicate that the testing procedures in the two laboratories gives consistent stress-strain response in the pre-necking range.

4.1.4. Carbon steel P110 (API Spec 5CT P110)

The P110 material was from a 9-7/8" seamless hot-rolled pipe section with wall thickness of 16.8 mm produced by Nippon Steel & Sumitomo Metal Corporation. The chemical composition is given in Table 2. As shown in Fig. 8, the three parallels at room temperature and the two parallels at 350 °C gives a consistent response, while the two parallels at 500 °C display a difference in stress level and strain at incipient necking. However, one of the tests at 350 °C display a rugged curve in for strains less than 0.01 due to slip in the extensometer in the initial stage of loading. According to API 5CT (American Petroleum Institute, 2011), the P110 have a specified yield strength of 758-965 MPa and a minimum tensile strength of 862 MPa at room temperature. As can be seen from Table 6, the tested material is within the specifications. Similar to the other carbon steels, the strength and total elongation at necking is significantly reduced for increased temperature. Assuming a thermal expansion of 12 μ/°C, a temperature increase of 500 °C will lead to 0.6% strain, which is close to the A_{gt} values of P110 at 500 °C.

4.1.5. Summary carbon steels

The average values of the yield strength ($R_{p0.2}$), the tensile strength (R_m) and the total engineering strain at necking (A_{gt}) for the steel alloys are given in Fig. 9. As expected, the K55 stands out from the other steels by having a lower yield strength at temperatures up to 350 °C. The K55 material also stands out from the other materials by displaying more work-hardening up to 350 °C, as can be seen by the relatively large tensile strength values compared to the yield strength for this material in Fig. 9. At temperatures of 500 °C and 550 °C, none of the carbon steels display much work hardening, while the tests performed at 450 °C show intermediate work hardening. Notably the T95 work hardens more at 250 °C and 350 °C than at room temperature. This is likely due to the yield plateau, which is present only in the room temperature tests, see Fig. 7. The strain at onset of necking (A_{gt}), is significantly reduced for temperatures above 250 °C and is higher for K55 than for the other steels.

4.2. Corrosion resistant alloys

4.2.1. Nickel based alloy 600 (UNS N06600)

The 600 specimens were cut from a 12.4 mm thick plate produced by Allegheny Technologies Incorporated (ATI). The chemical composition is given in Table 2.

As shown in Fig. 10, all parallel tests at given temperatures provide consistent pre-necking stress-strain response. The strength decreases for increased temperature, while the strain at onset of necking is somewhat

Table 4

Proof strength ($R_{p0.2}$), tensile strength (R_m), strain at onset of necking (A_{gt}) for the L80 material. The yield strength factor (YFS), tensile strength factor (TSF) and elongation factor (EF) are given based on the average $R_{p0.2}$, R_m and A_{gt} values.

Material	Temp.	Parallel	$R_{p0.2}$	R_m	A_{gt}	YSF	TSF	EF
L80	RT	1	620	741	0.082			
		2	621	747	0.080			
		Avg.	621	744	0.081	1.00	1.00	1.00
	250 °C	1	535	657	0.072			
		2	537	658	0.067			
		Avg.	536	657	0.070	0.86	0.88	0.86
	450 °C	1	481	562	0.049			
		2	473	562	0.047			
		Avg.	477	562	0.048	0.77	0.76	0.60
	550 °C	1	392	434	0.017			
		2	388	424	0.016			
		Avg.	390	429	0.017	0.63	0.58	0.21

Table 5

Proof strength ($R_{p0.2}$), tensile strength (R_m), strain at onset of necking (A_{gt}) for the T95 material. The yield strength factor (YFS), tensile strength factor (TSF) and elongation factor (EF) are given based on the average $R_{p0.2}$, R_m and A_{gt} values.

Material	Temp.	Parallel	$R_{p0.2}$	R_m	A_{gt}	YSF	TSF	EF
T95A	RT	1	687	802	0.092			
		2	688	801	0.090			
		Avg.	688	801	0.091	1.00	1.00	1.00
	350 °C	1	555	710	0.071			
		2	555	715	0.073			
		Avg.	555	713	0.072	0.81	0.89	0.80
	500 °C	1	457	501	0.020			
		2	476	536	0.030			
		Avg.	466	519	0.025	0.68	0.65	0.27
T95B	RT	1	726	844	0.084			
		2	726	842	0.087			
		Avg.	726	843	0.086	1.00	1.00	1.00
	250 °C	1	625	792	0.087			
		2	624	793	0.094			
		Avg.	625	793	0.090	0.86	0.94	1.05
	450 °C	1	543	657	0.053			
		2	544	659	0.052			
		Avg.	543	658	0.053	0.75	0.78	0.61
	550 °C	1	457	527	0.024			
		2	481	530	0.022			
		Avg.	469	528	0.023	0.65	0.63	0.27

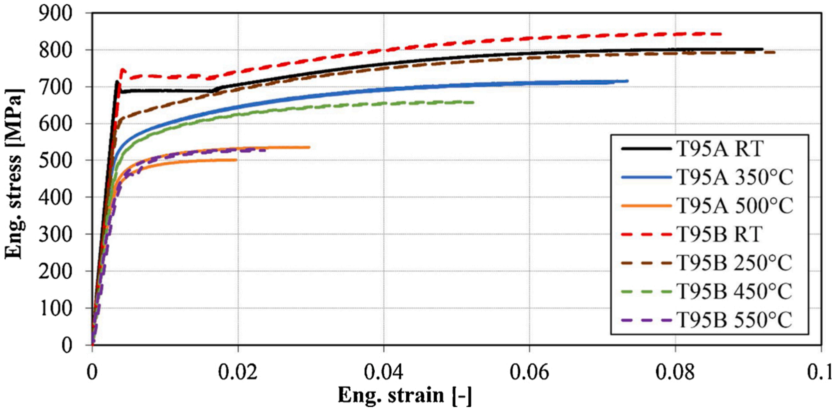

Fig. 7. Engineering stress-strain curves from all tensile tests on the T95 material. The results marked T95A are from samples tested at SINTEF, while the T95B results are from TNO.

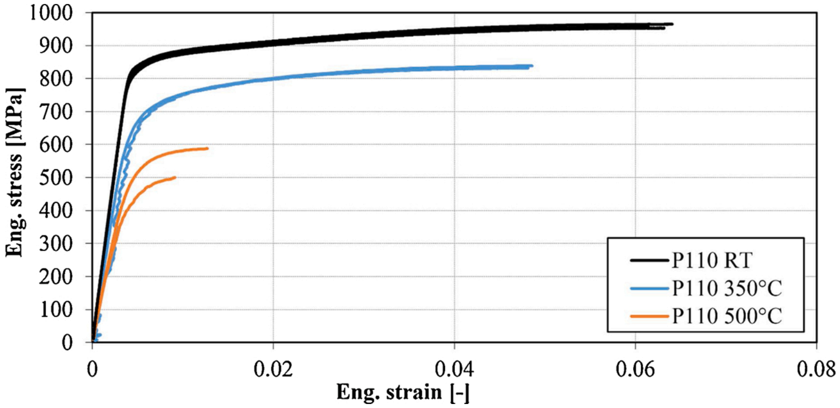

Fig. 8. Engineering stress-strain curves from all tensile tests on the P110 material.

larger at 350 °C than at room temperature and 500 °C. The tests performed at 350 °C and 500 °C display serrated curves due to the Portevin-LeChateliers effect (PLC). PLC occurs with dynamic strain ageing at material specific combinations of temperature and strain rate and is created by pinning and unpinning of dislocations (Abbadi et al., 2002). Table 7 compiles data from the tensile tests on the 600 alloy.

4.2.2. *Nickel based alloy 625 (UNS N06625)*

The 625A material tested at SINTEF was provided by ATI. The specimens were cut from a plate with thickness 10.9 mm. The 625B

Table 6
Proof strength ($R_{p0.2}$), tensile strength (R_m), strain at onset of necking (A_{gt}) for the P110 material. The yield strength factor (YFS), tensile strength factor (TSF) and elongation factor (EF) are given based on the average $R_{p0.2}$, R_m and A_{gt} values.

Material	Temp.	Parallell	$R_{p0.2}$	R_m	A_{gt}	YSF	TSF	EF
P110	RT	1	849	956	0.061			
		2	842	953	0.063			
		3	855	964	0.064			
		Avg.	848	958	0.063	1.00	1.00	1.00
	350°C	1	708	832	0.048			
		2	699	838	0.049			
		Avg.	704	835	0.048	0.83	0.87	0.77
	500°C	1	542	587	0.013			
		2	463	500	0.009			
		Avg.	502	544	0.011	0.59	0.57	0.17

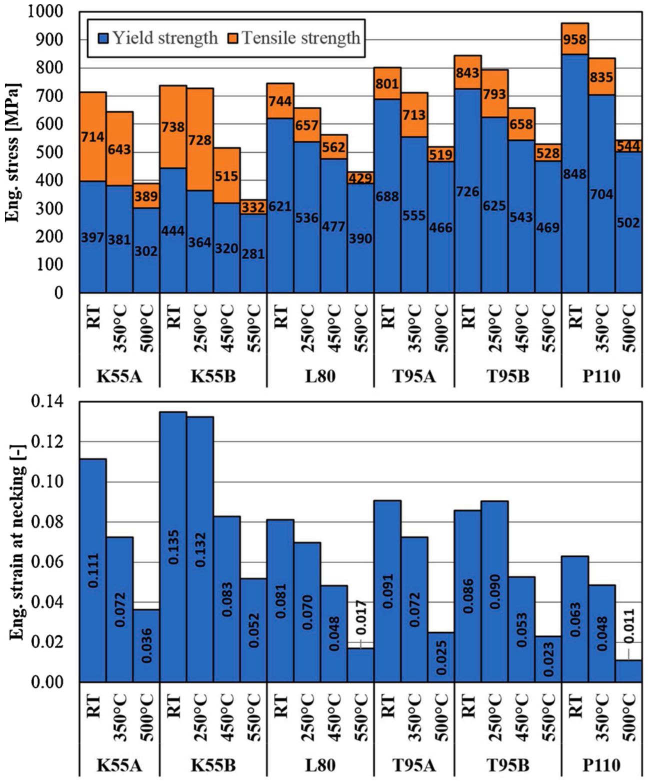

Fig. 9. Average values of yield strength ($R_{p0.2}$), tensile strength (R_m) and total engineering strain at necking (A_{gt}) of the tested carbon steels.

material tested at TNO came from Industeel ArcelorMittal and were cut from a plate with a 13.8 mm thickness. The chemical composition of 625A and 625B is given in Table 2.

At room temperature the stress-strain response of 625A and 625B is very similar. The tensile strength of the 625B material is reduced somewhat more than the 625A material, but in general the two alloys have a similar response at elevated temperature. The 625 material display a serrated curve at 250 °C due to the PLC effect. For higher temperatures the PLC effect is more pronounced as indicated in Fig. 11. Table 8 show data from the tensile tests on the 625A and 625B alloys.

4.2.3. *Nickel based alloy 800 (UNS N08810)*

The specimens of the 800 material were cut from a 6.7 mm thick plate produced by Allegheny Technologies Incorporated (ATI). The chemical composition is given in Table 2.

As shown in Fig. 12, the parallel tests at given temperatures give consistent stress-strain response. The tests performed at 350 °C and 500 °C display serrated flow due to the PLC effect and the same stress level at onset of yielding. The material work hardens more at 350 °C than at 500 °C. The elongation at onset of necking is higher at room temperature and 350 °C than at 500 °C. A summary of the data from tensile tests on the 800 alloy is given in Table 9.

4.2.4. *Nickel based alloy C276 (UNS N10276)*

The C276 material was produced by ATI. The specimens were cut from a plate with 10 mm thickness. The chemical composition is given in Table 2.

As shown in Fig. 13, all parallel tests at given temperatures give consistent stress-strain response. The tests performed at 350 °C and 500 °C display the PLC effect. The recordings of the two 350 °C parallels were corrupted before necking, thus the last part of the curves is not shown in Fig. 13, and the associated values in Table 10 are lower bound.

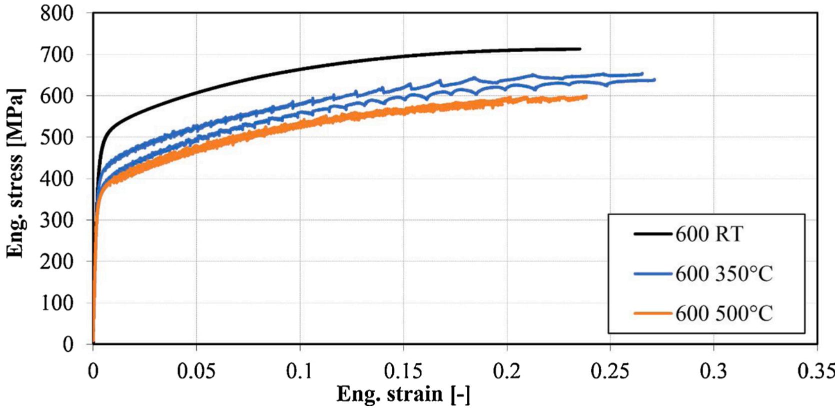

Fig. 10. Engineering stress-strain curves from all tensile tests on the 600 material.

Table 7

Proof strength ($R_{p0.2}$), tensile strength (R_m), strain at onset of necking (A_{gt}) for the 600 material. The yield strength factor (YFS), tensile strength factor (TSF) and elongation factor (EF) are given based on the average $R_{p0.2}$, R_m and A_{gt} values.

Material	Temp.	Parallell	$R_{p0.2}$	R_m	A_{gt}	YSF	TSF	EF
600	RT	1	480	713	0.235			
		2	478	712	0.234			
		Avg.	479	712	0.234	1.00	1.00	1.00
	350°C	1	373	639	0.271			
		2	410	654	0.265			
		Avg.	392	646	0.268	0.82	0.91	1.15
	500°C	1	358	600	0.238			
		2	364	578	0.198			
		Avg.	361	589	0.218	0.75	0.83	0.93

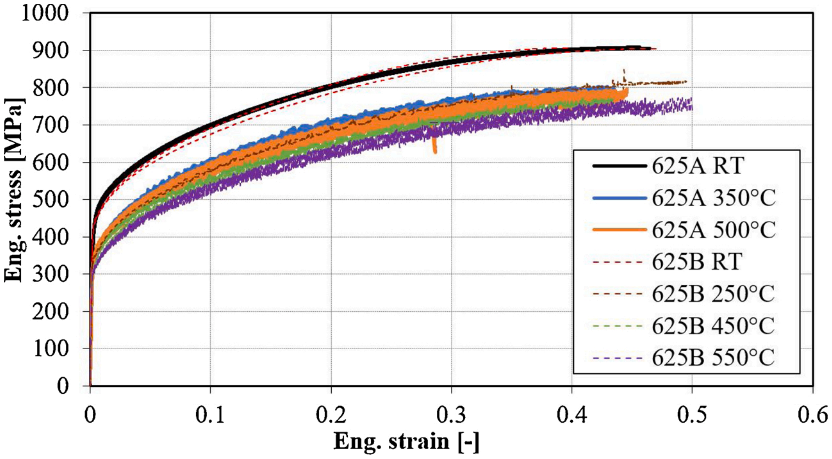

Fig. 11. Engineering stress-strain curves from all tensile tests on the 625A and 625B materials.

Table 8

Proof strength ($R_{p0.2}$), tensile strength (R_m), strain at onset of necking (A_{gt}) for the 625 materials. The yield strength factor (YFS), tensile strength factor (TSF) and elongation factor (EF) are given based on the average $R_{p0.2}$, R_m and A_{gt} values.

Material	Temp.	Parallell	$R_{p0.2}$	R_m	A_{gt}	YSF	TSF	EF
625A	RT	1	451	908	0.456			
		2	444	905	0.465			
		Avg.	448	907	0.460	1.00	1.00	1.00
	350 °C	1	346	795	0.430			
		2	339	802	0.435			
		Avg.	342	798	0.432	0.77	0.88	0.94
	500 °C	1	355	787	0.398			
		2	351	797	0.446			
		Avg.	353	792	0.422	0.79	0.87	0.92
625B	RT	1	444	907	0.396			
		2	444	905	0.471			
		Avg.	444	906	0.433	1.00	1.00	1.00
	250 °C	1	352	815	0.495			
		2	351	816	0.481			
		Avg.	352	815	0.488	0.79	0.90	1.13
	450 °C	1	322	758	0.435			
		2	327	735	0.365			
		Avg.	325	747	0.400	0.73	0.82	0.92
	550 °C	1	313	739	0.500			
		2	325	733	0.468			
		Avg.	319	736	0.484	0.72	0.81	1.12

4.2.5. Austenitic stainless steel 6Mo (UNS S31254)

The 6Mo material was from a seamless pipe section with 6-5/8″ outer diameter and 18 mm wall thickness produced by Tubacex. The chemical composition is given in Table 2.

As shown in Fig. 14, all parallel tests at given temperatures give consistent stress-strain response. Notably, there is a significant drop in strength from room temperature to 350 °C, but not a large difference is strength between the tests performed at 350 °C and 500 °C. However, the tests performed at 500 °C display serrated curves due to the PLC effect. This effect is to some extent also present in the tests performed at 350 °C. The two parallels performed at 500 °C experienced a slip in one of the fixtures prior to necking, thus the last part of the stress-strain curve in these tests are not shown in Fig. 14, and the associated values in Table 11 are lower bound.

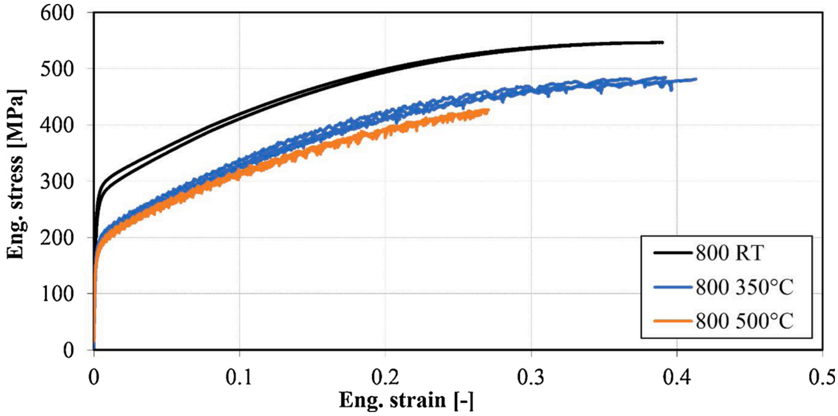

Fig. 12. Engineering stress-strain curves from all tensile tests on the 800 material.

Table 9
Proof strength ($R_{p0.2}$), tensile strength (R_m), strain at onset of necking (A_{gt}) for the 800 material. The yield strength factor (YSF), tensile strength factor (TSF) and elongation factor (EF) are given based on the average $R_{p0.2}$, R_m and A_{gt} values.

Material	Temp.	Parallell	$R_{p0.2}$	R_m	A_{gt}	YSF	TSF	EF
800	RT	1	276	546	0.383			
		2	256	546	0.390			
		Avg.	266	546	0.387	1.00	1.00	1.00
	350°C	1	190	485	0.392			
		2	182	478	0.396			
		3	188	482	0.413			
		Avg.	187	481	0.401	0.70	0.88	1.04
	500°C	1	172	427	0.271			
		2	179	427	0.270			
		Avg.	175	427	0.270	0.66	0.78	0.70

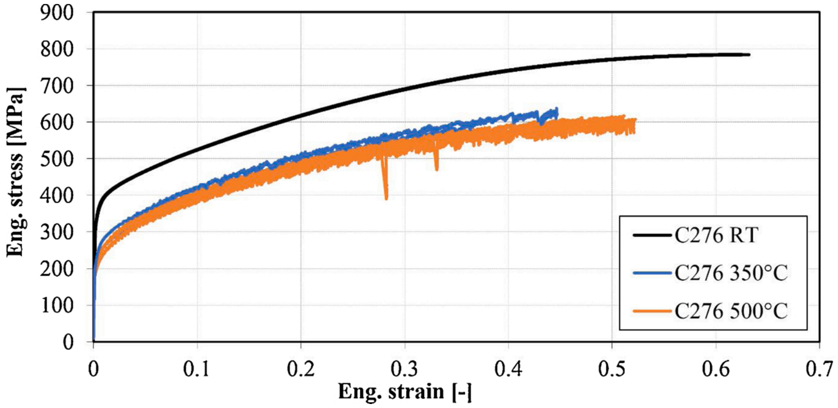

Fig. 13. Engineering stress-strain curves from all tensile tests on the C276 material.

Table 10
Proof strength ($R_{p0.2}$), tensile strength (R_m), strain at onset of necking (A_{gt}) for the C276 material. The yield strength factor (YSF), tensile strength factor (TSF) and elongation factor (EF) are given based on the average $R_{p0.2}$, R_m and A_{gt} values.

Material	Temp.	Parallell	$R_{p0.2}$	R_m	A_{gt}	YSF	TSF	EF
C276	RT	1	353	784	0.625			
		2	343	783	0.632			
		Avg.	348	784	0.628	1.00	1.00	1.00
	350 °C	1	222	>592	>0.362			
		2	234	>637	>0.446			
		Avg.	228	>637	>0.446	0.66	>0.81	>0.71
	500 °C	1	200	607	0.522			
		2	209	617	0.511			
		Avg.	205	612	0.517	0.59	0.78	0.82

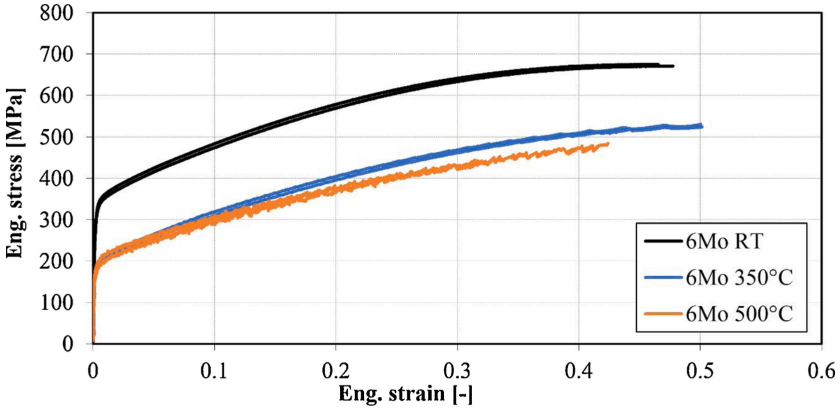

Fig. 14. Engineering stress-strain curves from all tensile tests on the 6Mo material.

Table 11

Proof strength ($R_{p0.2}$), tensile strength (R_m), strain at onset of necking (A_{gt}) for the 6Mo material. The yield strength factor (YFS), tensile strength factor (TSF) and elongation factor (EF) are given based on the average $R_{p0.2}$, R_m and A_{gt} values.

Material	Temp.	Parallell	$R_{p0.2}$	R_m	A_{gt}	YSF	TSF	EF
6Mo	RT	1	321	671	0.477			
		2	330	675	0.465			
		Avg.	326	673	0.471	1.00	1.00	1.00
	350 °C	1	193	530	0.500			
		2	186	524	0.501			
		Avg.	189	527	0.501	0.58	0.78	1.06
	500 °C	1	193	>442	>0.320			
		2	174	>484	>0.424			
		Avg.	183	>484	>0.424	0.56	>0.72	>0.90

4.2.6. *Titanium alloy Ti23 (ASTM Grade 23)*

The titanium alloy was from a 40 mm thick pipe section provided to SINTEF by Equinor, industrial partner in the HotCaSe project. Material specifications did not follow, but the tested chemical composition and the proof- and tensile stress at room temperature is in line with Grade 23 as defined by ASTM B862 (ASTM International, 2019).

As shown in Fig. 15, there is a significant drop in strength from room temperature to 350 °C, while the tests performed at 350 °C and 500 °C have similar strength. However, the tests performed at 500 °C have a significantly lower strain at necking than the tests performed at room temperature and 350 °C. In contrast to the other CRA materials in this study, the Ti23 does not show dynamic strain ageing. Table 12 provides a summary of the data from the tensile tests.

4.2.7. *Summary CRA materials*

Fig. 16 shows the average $R_{p0.2}$, R_m and A_{gt} values for the CRA casing materials. The general behaviour of the nickel-based alloys and the 6Mo stainless steel (which is alloyed by a substantial amount of nickel) is similar, while the Ti23 alloy stands out. The nickel alloyed materials in Fig. 16 display significant work hardening and large values of strain at necking for all tested temperatures. In particular, the 625 material have high values of all three parameters ($R_{p0.2}$, R_m and A_{gt}). The Ti23 alloy have response parameters in the same range as the P110 steel within the tested temperatures, although the strength at 350 °C is lower and the elongation at necking is higher, particularly at 500 °C.

5. Discussion

In NZS 2403:2015 the reduction of yield strength as function of temperature (YSF) is given separately for J55/K55 grades and for L80/C90/T95 grades, while the tensile strength factor (TSF) is given as average for all grades. In the following we will occasionally refer to K55

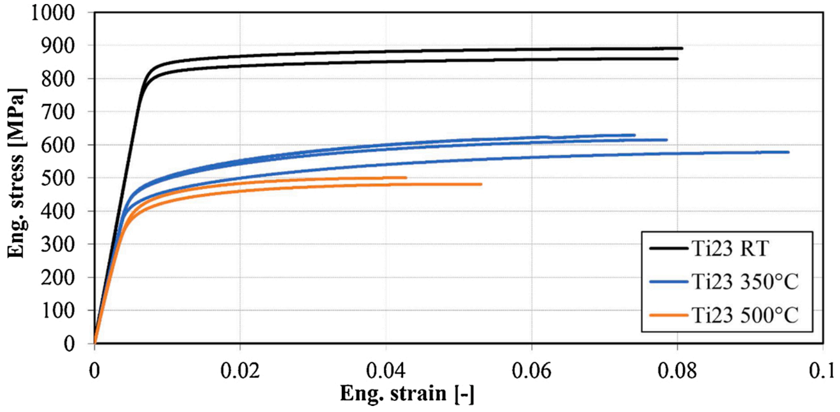

Fig. 15. Engineering stress-strain curves from all tensile tests on the titanium material.

Table 12
Proof strength ($R_{p0.2}$), tensile strength (R_m), strain at onset of necking (A_{gt}) for the Ti23 material. The yield strength factor (YFS), tensile strength factor (TSF) and elongation factor (EF) are given based on the average $R_{p0.2}$, R_m and A_{gt} values.

Material	Temp.	Parallell	$R_{p0.2}$	R_m	A_{gt}	YSF	TSF	EF
Ti23	RT	1	840	891	0.081			
		2	809	860	0.080			
		Avg.	825	875	0.080	1.00	1.00	1.00
	350 °C	1	468	615	0.078			
		2	430	578	0.095			
		3	476	629	0.074			
		Avg.	458	607	0.083	0.56	0.69	1.03
	500 °C	1	416	500	0.043			
		2	394	481	0.053			
		Avg.	405	491	0.048	0.49	0.56	0.60

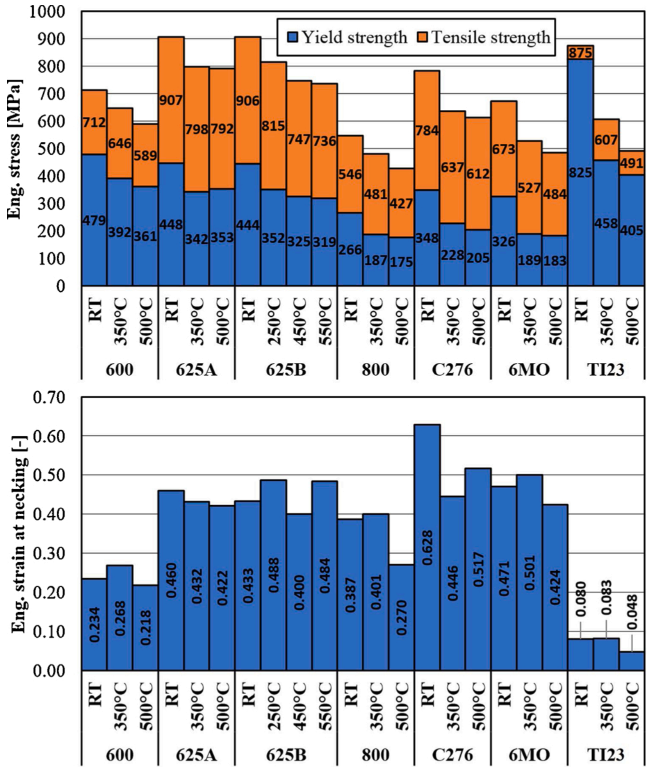

Fig. 16. Average values of the yield strength ($R_{p0.2}$), tensile strength (R_m) and total engineering strain at necking (A_{gt}) of the tested nickel based alloys, the austenitic stainless steel and the titanium alloy.

as a lower strength steel and to L80, T95 and P110 as higher strength steels. The YSF and the TSF from the K55 materials tested in the present study are shown along the data from NZS 2403:2015 in Fig. 17. The YSF of the K55B material decreases with increasing temperature with a similar rate as the NZS 2403:2015 curve, while the K55A material shows only a small reduction in YSF at 350 °C. The latter is related to the lack of yield plateau in the K55A material, which result in lower yield strength and therefore relatively high YSF at higher temperature. The TSF of the K55A material is near the NZS 2403:2015 value at 350 °C, and then drops significantly when increasing the temperature to 500 °C. The K55B material displays a very high tensile strength at 250 °C but shows the same trend as the K55A material for temperatures of 450 °C and above. Overall, the results from the tested K55 materials supports the YSF and TSF of the NZS 2403:2015. Further, the results indicate that the decrease in yield strength up to 550 °C follows the same rate as up to 350 °C, while the tensile strength display a significant drop for temperatures above 400 °C.

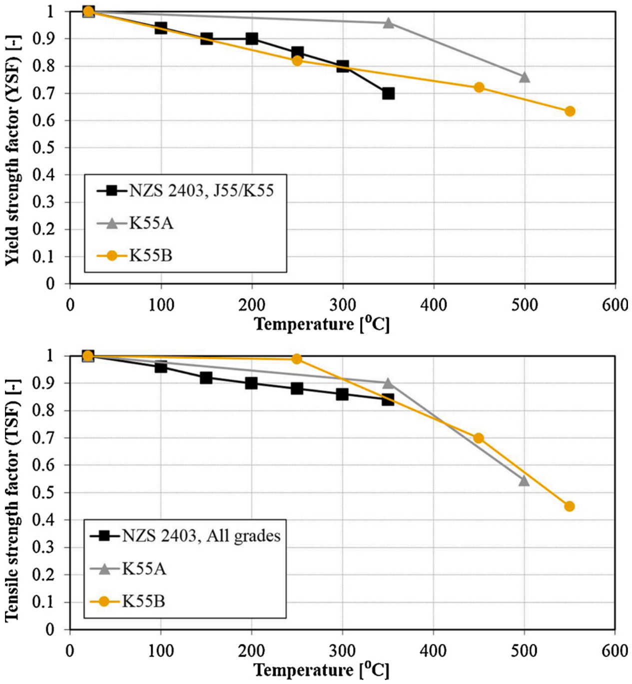

Fig. 17. Yield strength factor (YSF) and tensile strength factor (TSF) from the tested K55 steel and results from NZS 2403:2015.

In Fig. 18, the yield strength factor and the tensile strength factor from the higher strength steels tested in the present study are compared with the YSF and TSF from the NZS 2403:2015. As can be seen from Fig. 18, both the YTS and TSF from the present study follows the NZS 2403:2015 curves up to 350 °C. The tested higher strength steels indicate a near constant rate in YSF for temperatures up to 550 °C, however, the P110 loose more strength than the other steels. The deterioration rate of the TSF increase for temperatures above 450 °C, but not to the same extent as for the K55. Also here the deterioration of the P110 material is higher than in the other steels at 500 °C.

The yield- and tensile strength factors for the tested nickel-based alloys and the 6Mo and Ti23 alloys are shown in Fig. 19. The NZS 2403:2015 data for carbon steels are also provided in Fig. 19 for reference. The tensile strength factor of the nickel-based alloys follows the deterioration trend of the carbon steels up to 350 °C, but in contrast to the carbon steels tested in the present study, tend to flatten for higher temperatures. The reduction in YSF for the 6Mo and the Ti23 alloys is higher than for the carbon steels up to 350 °C, but also these materials retain yield strength for higher temperatures. The tensile strength factor for the nickel-based alloys and the 6Mo deteriorates with the same rate as the carbon steels up to 350 °C and in general follows the same deterioration rate for higher temperatures. On the other side, the TSF of the Ti23 alloy display a linear reduction at a significantly higher rate.

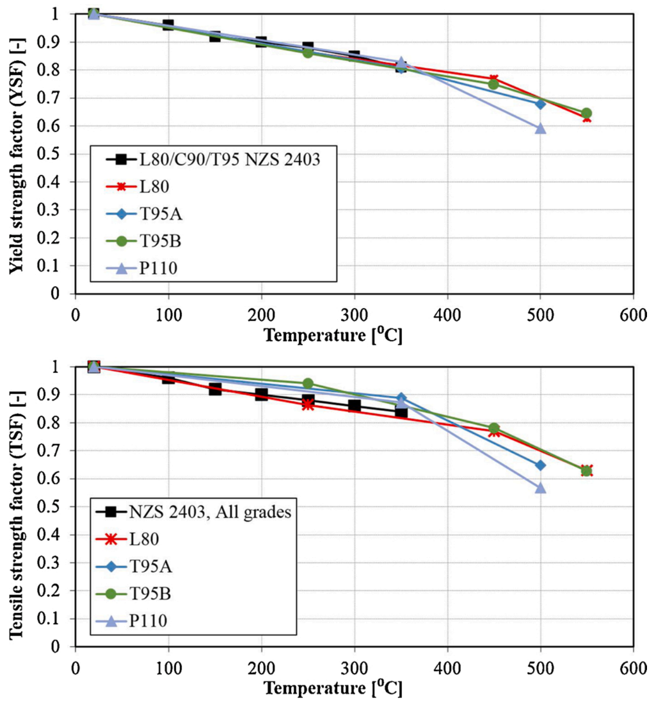

Fig. 18. Yield strength factor (YSF) and tensile strength factor (TSF) from the tested higher strength steels and results from NZS 2403:2015.

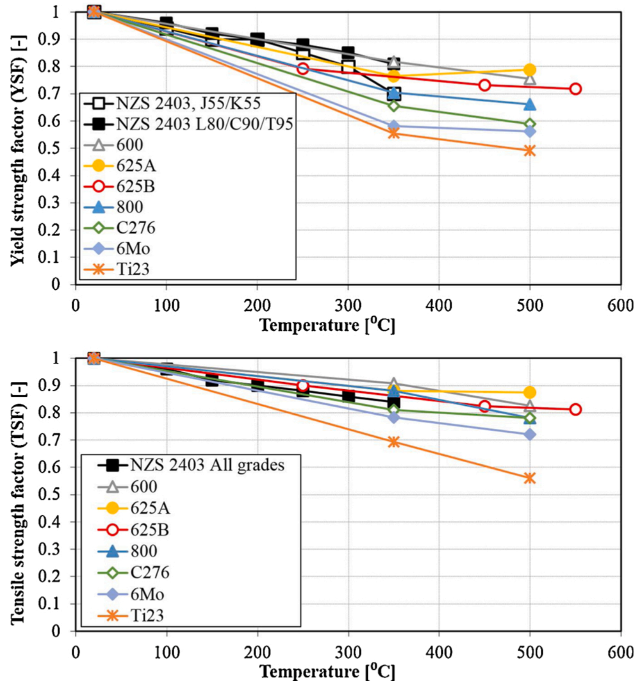

Fig. 19. Yield strength factor (YSF) and tensile strength factor (TSF) from the tested nickel-based alloys, the austenitic steel and the titanium alloy. The carbon steel results from NZS 2403:2015 are given for reference.

The serrated stress-strain behaviour at higher temperature in the nickel-based alloys and the austenitic steel is explained by the PLC effect or dynamic strain aging. Dynamic strain ageing can accelerate the deterioration of the material under low-cycle fatigue (Mannan, 1993, Hong and Lee, 2004, Hongwei et al., 2014). Well discharges will induce cyclic loading on the well, thus separate studies must be conducted before these materials are applied as structural components in casing design where plastic deformation can occur. However, the materials could still be part of the design as a corrosive protective cladding. The Ti23 alloy display yield- and tensile strength properties similar to the P110 steel and is in contrast to the other CRA materials not exposed to dynamic strain ageing. In combination with a low Young's modulus and low thermal expansion, this makes the Ti23 material from a mechanical point of view an interesting alternative as a structural material in ultra-high geothermal wells.

One material property that is important in an ultra-high temperature casing is creep. During operation, compressive stresses will be lower due to relaxation and so the casing will be in a better position to withstand tensile stresses that occurs during a well discharge. On the other hand, a high-grade casing exposed to this temperature range (e.g. above 450 °C) can be influenced by metallurgical ageing which reduce the yield- and tensile strength thus making the casing more prone to tensile failure during a shut-down. The creep- and ageing effects illustrates the increased complexity on the material level that must be dealt with when moving into ultra-high temperature design, as well as knowledge gaps that remain as future work.

6. Conclusions

The stress-strain response of 4 types of carbon steel and 6 types of CRA materials are investigated for temperatures in the range from room temperature up to 550 °C. The tests have been performed by two different laboratories at SINTEF and TNO and the results in the pre-necking range are in good agreement. The experiments extend the existing literature by providing data for higher temperatures and different material classes and can be applied in design of collapse-, burst- and compressive/tensile capacity of casings for high- to ultra-high temperature geothermal wells. The deterioration of the yield- and tensile strength of the carbon steels follows the trend shown in NZS 2403:2015 up to 350 °C. I.e. the yield- and tensile strength are reduced to ~80 % and ~85 %, respectively at 350 °C as compared to the strength at room temperature. For higher temperatures, the yield- and tensile strength continues to decrease with the same rate and is reduced to ~60 % at 550 °C for all carbon steels except for the K55 steel where a significant drop in tensile strength occurs. At 550 °C, the tensile strength of the K55 steel is reduced to ~45 % of the capacity at room-temperature. A Lüders plateau was observed at room temperature in three of the carbon steels, but not at higher temperatures. The K55 steel from one producer had Lüders plateau, while the K55 steel from the other producer did not. This could be related to differences in alloy composition, heat treatment, strain rate or a combination of all three. It is pointed out that both relaxation and metallurgical ageing are effects that must be considered in casing design in the ultra-high temperature range, but these effects are not within the scope of the present work.

The alloys with high nickel content work hardens significantly more than the carbon steels at elevated temperatures and they tend to retain the strength for temperatures above 350 °C. However, these alloys display dynamic strain ageing which might qualify them only as corrosive protective cladding in a casing solution, but more research must be conducted before a clear conclusion is drawn. The tested titanium alloy shows high strength at 500 °C and have no PLC effect. Based on collapse- and tensile capacity, this material is a casing candidate for ultra-high temperature wells.

CRediT authorship contribution statement

Gaute Gruben: Writing - original draft, Formal analysis, Data curation. **Bert Dillingh:** Formal analysis, Data curation. **Gunnar Skúlason Kaldal:** Data curation, Writing - review & editing. **Nguyen- Hieu Hoang:** Funding acquisition, Data curation. **Jens Wollenweber:** Funding acquisition, Project administration. **Gisle Rørvik:** Conceptualization, Data curation. **Ingólfur Thorbjornsson:** Conceptualization, Data curation. **Bård Nyhus:** Conceptualization, Formal analysis, Data curation.

Declaration of Competing Interest

The authors report no declarations of interest.

Acknowledgements

The authors would like to thank both the HotCaSe project and the H2020 GeoWell project for their financial support and provided experimental data for publication. The GeoWell project is supported from the EU Horizon 2020 programme with grant agreement number No 654497 while the HotCaSe project is supported from the Norwegian Research Council with grant number NFR269399.

References

Abbadi, M., Hähner, P., Zeghloul, A., 2002. On the characteristics of Portevin–Le Chatelier bands in aluminum alloy 5182 under stress-controlled and strain-controlled tensile testing. Materials Science and Engineering: A 337, 194–201.

Albertini, C., Montagnani, M., 1977. Dynamic material properties of several steels for fast breeder reactor safety analysis. Joint Research Centre Ispra Establishment.

American Petroleum Institute, 2011. API Specification 5CT.

Ármannsson, H., Fridriksson, T., Gudfinnsson, G.H., Ólafsson, M., Óskarsson, F., Thorbjörnsson, D., 2014. IDDP—The chemistry of the IDDP-01 well fluids in relation to the geochemistry of the Krafla geothermal system. Geothermics 49, 66–75.

ASTM International, 2017. Standard Test Methods for Elevated Temperature Tension Tests of Metallic Materials.

ASTM International, 2019. ASTM B862. Standard Specification for Titanium and Titanium Alloy Welded Pipe.

Dillingh, B., Kaldal, G.S., Thorbjornsson, I., Wollenweber, J., Vercauteren, F., 2020. Tensile Testing of Casing Material at Elevated Temperatures Up to 550°C. In: World Geothermal Congress 2020. Reykjavík.

Elders, W.A., Friðleifsson, G.Ó., Albertsson, A., 2014. Drilling into magma and the implications of the Iceland Deep Drilling Project (IDDP) for high-temperature geothermal systems worldwide. Geothermics 49, 111–118.

Friðleifsson, G.Ó., Elders, W.A., Albertsson, A., 2014. The concept of the Iceland deep drilling project. Geothermics 49, 2–8.

Hong, S.-G., Lee, S.-B., 2004. The tensile and low-cycle fatigue behavior of cold worked 316L stainless steel: influence of dynamic strain aging. International Journal of Fatigue 26, 899–910.

Hongwei, Z., Yizhu, H., Jizu, L., Sixian, R., 2014. Study on Dynamic Strain Aging and Low-Cycle Fatigue of Stainless Steel in Ultra-Supercritical Unit. Energy Materials 2014. Springer, Cham.

Ingason, K., Árnason, A.B., Bóasson, H.Á., Sverrisson, H., Sigurjónsson, K.Ö., Gíslason, P., 2015. IDDP-2, Well design. In: World Geothermal Congress 2015. Melbourne, Australia.

International Organization for Standardization, 2016. ISO 6892-1:2016. Metallic materials — Tensile testing — Part 1: Method of test at room temperature.

International Organization for Standardization, 2018. ISO 6892-2:2018. Metallic materials — Tensile testing — Part 2: Method of test at elevated temperature.

Kaldal, G., Jonsson, M., Pálsson, H., Karlsdottir, S., 2015. Structural Analysis of Casings in High Temperature Geothermal Wells in Iceland.

Kaldal, G.S., 2019. Nonlinear Finite-Element Analysis of Casings in High-Temperature Geothermal Wells. PhD, University of Iceland.

Kaldal, G.S., Jonsson, M.T., Palsson, H., Karlsdottir, S.N., 2016. Structural modeling of the casings in the IDDP-1 well: Load history analysis. Geothermics 62, 1–11.

Kaldal, G.S., Thorbjornsson, I.O., 2016. Thermal expansion of casings in geothermal wells and possible mitigation of resultant axial strain. In: European Geothermal Congress 2016. Strasbourg, France.

Karlsdottir, S.N., Ragnarsdottir, K.R., Thorbjornsson, I.O., Einarsson, A., 2015. Corrosion testing in superheated geothermal steam in Iceland. Geothermics 53, 281–290.

Knight, C.L., Bodnar, R.J., 1989. Synthetic fluid inclusions: IX. Critical PVTX properties of NaCl-H2O solutions. Geochimica et Cosmochimica Acta 53, 3–8.

Mannan, S.L., 1993. Role of dynamic strain ageing in low cycle fatigue. Bulletin of Materials Science 16, 561–582.

New Zealand Standard, 2015. NZS: 2403:2015 Code of practice for deep geothermal wells.

Rechard, R.P., Schuler, K.W., 1983. Euler Buckling of Geothermal Well Casing. Sandia National Laboratories.

SAE, ASTM, 2017. Metals & Alloys in the Unified Numbering System, 13th Edition.

Seely, F.B., Putnam, W., 1919. The relation between the elastic strengths of steel in tension, compression and shear. University of Illinois bulletin 17, 3–49.

Thorbjornsson, I.O., Kaldal, G.S., Gunnarsson, B.S., Ragnarsson, Á., 2017. A New Approach to Mitigate Casing failures in High-Temperature Geothermal Wells. In: Geothermal Resources Council 41st Annual Meeting. Salt Lake City.

Thorbjornsson, I.O., Kaldal, G.S., Krogh, B.C., Palsson, B., Markusson, S.H., Sigurdsson, P., Einarsson, A., Gunnarsson, B.S., Jonsson, S.S., 2020. Materials Investigation of the High Temperature IDDP-1 Wellhead Geothermics. accepted for publication.

Thórhallsson, S., Pálsson, B., Hólmgeirsson, S., Ingason, K., Matthíasson, M., Bóasson, H.Á., Sverrisson, H., 2014. Well design for the Iceland Deep Drilling Project (IDDP). Geothermics 49, 16–22.